Research Article
doi.org/10.1002/cctc.202300871
Chemistry Europe
European Chemical Societies Publishing

www.chemcatchem.org

Macrocyclization of Dienes under Confinement with Cationic Tungsten Imido/Oxo Alkylidene *N*-Heterocyclic Carbene Complexes

Felix Ziegler,[a] Johanna R. Bruckner,[b] Michal Nowakowski,[c] Matthias Bauer,[c] Patrick Probst,[a] Boshra Atwi,[a] and Michael R. Buchmeiser*[a]

Macrocyclization reactions are still challenging due to competing oligomerization, which requires the use of small substrate concentrations. Here, the cationic tungsten imido and tungsten oxo alkylidene *N*-heterocyclic carbene complexes [[W(N-2,6-Cl_2-C_6H_3)($CHCMe_2Ph$(OC_6F_5)(pivalonitrile)(IMes)$^+$ $B(Ar^F)_4^-$] (**W1**) and [W(O)($CHCMe_2Ph$($OCMe(CF_3)_2$)(IMes)(CH_3CN)$^+$ $B(Ar^F)_4^-$] (**W2**) (IMes = 1,3-dimesitylimidazol-2-ylidene; $B(Ar^F)_4^-$ = tetrakis(3,5-bis(trifluoromethyl)phenyl borate) have been immobilized inside the pores of ordered mesoporous silica (OMS) with pore diameters of 3.3 and 6.8 nm, respectively, using a pore-selective immobilization protocol. X-ray absorption spectroscopy of **W1@OMS** showed that even though the catalyst structure is contracted due to confinement by the mesopores, both the oxidation state and structure of the catalyst stayed intact upon immobilization. Catalytic testing with four differently sized α,ω-dienes revealed a dramatically increased macrocyclization (MC) and *Z*-selectivity of the supported catalysts compared to the homogenous progenitors, allowing high substrate concentrations of 25 mM. With the supported complexes, a maximum increase in MC-selectivity from 27 to 81% and in *Z*-selectivity from 17 to 34% was achieved. In general, smaller mesopores exhibited a stronger confinement effect. A comparison of the two supported tungsten-based catalysts showed that **W1@OMS** possesses a higher MC-selectivity, while **W2@OMS** exhibits a higher Z-selectivity which can be rationalized by the structures of the catalysts.

Introduction

Catalytic reactions under steric confinement, e.g. in mesoporous systems, mimic enzymes and benefit from the proximity of the catalyst to a pore wall with a defined geometry and polarity. This way, confinement can, e.g., induce a prefolding or preorientation of substrates and, thus, stabilize critical transition states which are difficult to realize otherwise.[1] This can lead to unexpected, sometimes unusually high[2] or inverted selectivities,[3] productivities, and activities.[4] Over the last years we have developed concepts to mimic enzymes by immobilizing well-defined organometallic catalysts inside mesoporous supports, thereby taking advantage of confinement effects. In fact, a catalyst placed inside a small pore adopts a "secondary structure", due to confinement, which allows for tuning a catalyst's reactivity and selectivity by tuning the relevant transition states in the catalytic cycle.[5]

We already reported on olefin metathesis-based macrocyclization (MC) reactions under confinement using both, modified Grubbs-Hoveyda-type and cationic molybdenum imido alkylidene *N*-heterocyclic carbene (NHC) catalysts.[5a–d,g,h,6] These catalysts were selectively immobilized inside the mesopores of SBA-15 and other ordered mesoporous silica (OMS) materials and allowed for macrocyclization (MC) reactions at concentrations of up to 100 mM with MC selectivities of up to 98%. In view of the peculiar reactivity and selectivity of tungsten imido or tungsten oxo alkylidene NHC catalysts[7] we were interested how the analogous tungsten-based catalysts would perform under these conditions and to which extent the concept of confined catalysts could be extended to another class of organometallic catalysts.

Results

Catalysts [W(N-2,6-Cl_2-C_6H_3)($CHCMe_2Ph$-(OC_6F_5)(pivalonitrile)(IMes)$^+$ $B(Ar^F)_4^-$][8] (**W1**) and [W-(O)($CHCMe_2Ph$($OCMe(CF_3)_2$)(IMes)(CH_3CN)$^+$ $B(Ar^F)_4^-$][7h] (**W2**, Figure 1) were prepared according to the literature. Two OMS materials with pore diameters of 3.3 nm and 6.8 nm, respectively, were prepared via true liquid crystal templating using hexadecylethyldimethylammonium bromide or P123, respec-

[a] Dr. F. Ziegler, P. Probst, B. Atwi, Prof. Dr. M. R. Buchmeiser
Institute of Polymer Chemistry
University of Stuttgart
Pfaffenwaldring 55, D-70569 Stuttgart (Germany)
E-mail: michael.buchmeiser@ipoc.uni-stuttgart.de

[b] Dr. J. R. Bruckner
Institute of Physical Chemistry
University of Stuttgart
Pfaffenwaldring 55, D-70569 Stuttgart (Germany)

[c] Dr. M. Nowakowski, Prof. Dr. M. Bauer
Department of Chemistry and Center for Sustainable Systems Design (CSSD)
Paderborn University
Warburger Str. 100, D-33098 Paderborn (Germany)

Supporting information for this article is available on the WWW under https://doi.org/10.1002/cctc.202300871

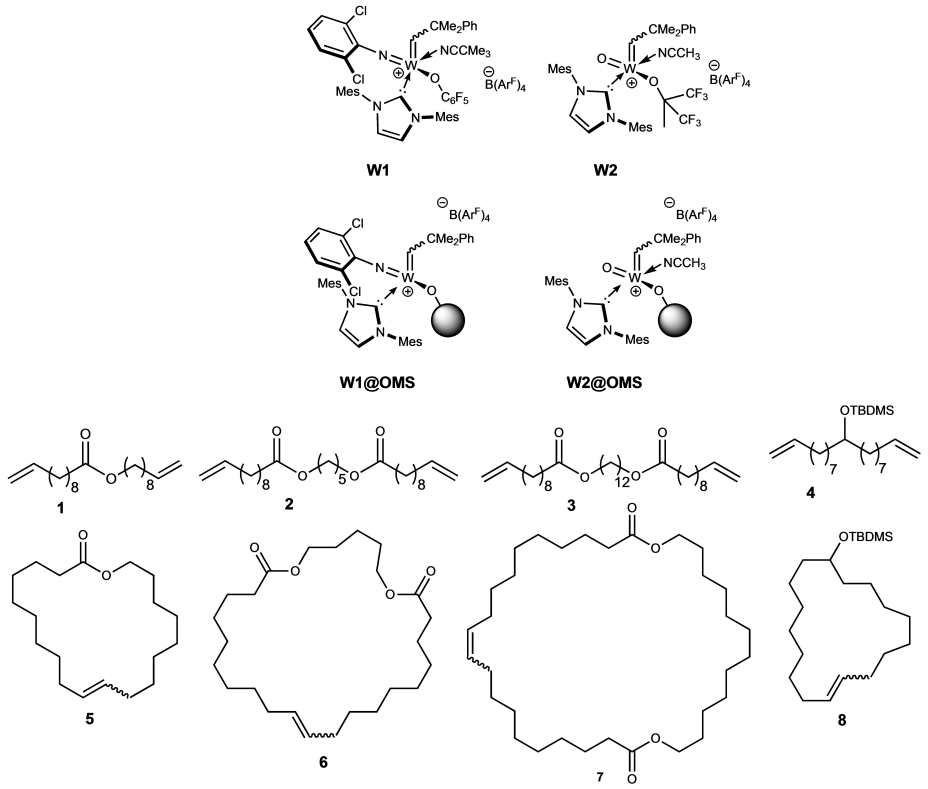

Figure 1. Structures of the parent catalysts W1 and W2, their supported versions W1@OMS and W2@OMS as well as of the substrates 1–4 and the macrocyclic products 5–8.

tively, as surfactant. Both OMS exhibited a hexagonal order of the mesopores and a narrow pore size distribution (cf. Figures S1–S3). The specific surface areas determined by the NLDFT method were 695 $m^2 g^{-1}$ for $OMS_{33Å}$ and 245 $m^2 g^{-1}$ for $OMS_{68Å}$. Pore-selective immobilization was accomplished following a protocol described earlier.[5b–d] Briefly, the mesopores of OMS were filled with the Pluronic® P123; then the outer surface of the OMS was reacted with hexamethyldisilazane (HMDS) for passivation (Figure 2). After removal of the Pluronic® with ethanol and thorough drying of the modified OMS, solutions of **W1** and **W2** in 1,2-dichlorobenzene were introduced into the mesopores and immobilized via substitution of the hexafluoro-*tert*-butoxide and pentafluorophenoxide ligand, respectively, by the surface silanol groups of the OMS to yield **W1@OMS** and **W2@OMS**, respectively (Figure 1). For both **W1** and **W2**, two OMS materials with different average pore diameters were used yielding in total four supported catalysts, **W1@OMS$_{33Å}$**, **W1@OMS$_{68Å}$**, **W2@OMS$_{33Å}$** and **W2@OMS$_{681Å}$**. Physisorption analysis after the immobilization process verified that the mean pore diameter as well as the pore size distribution of the support were only slightly altered during immobilization. (cf. Figures S4–S5, Table S2). Scanning electron microscopy analysis yielded particle sizes of roughly 3 to 300 μm for catalysts supported by **OMS$_{33Å}$** and 70 to 500 μm for catalysts supported by **OMS$_{68Å}$** (cf. Figure S6). The catalyst loadings for these four supported catalysts were 10.2 (**W1@OMS$_{33Å}$**), 16.5 (**W1@OMS$_{68Å}$**), 5.6 (**W2@OMS$_{33Å}$**) and 26.0 (**W2@OMS$_{68Å}$**) μmol/g. Even though the specific surface area of $OMS_{33Å}$ is more than twice as large as that of $OMS_{68Å}$, the catalyst loadings on $OMS_{68Å}$ are significantly larger. This effect may be rationalized by increasing diffusion limitations of **W1** and **W2** into the mesopores with decreasing pore sizes.[6,9]

Four α,ω-dienes were used as substrates for MC; these were dec-9-en-1-yl undec-10-enoate **1**,[5b,d,10] pentane-1,5-diyl bis(undec-10-enoate) **2**,[5b,d,10] dodecane-1,12-diyl bis(undec-10-enoate) **3**,[5d] and *tert*-butyldimethyl(nonadeca-1,18-dien-10-yloxy)silane **4**[5b,10] (Figure 1). To obtain the reference spectra of the macrocyclic products **5**–**8** (Figure 1), MC reactions were carried out at room temperature in CH_2Cl_2 using the 2nd-generation Grubbs catalyst $RuCl_2(PCy_3)(IMes)(CHPh)$. Where possible, the *E*/*Z* isomers were separated by semi-preparative HPLC. MC reactions with catalysts **W1** and **W2** were carried out in C_6D_6 using stock solutions of the corresponding catalyst in $CDCl_3$. Both conversion and the macrocycle:oligomer (MC:O) ratios were determined by ^{1}H NMR as described earlier.[5b,d] Exemplary ^{1}H NMR spectra are shown in Figures S7–S10. Table 1 summarizes the results obtained.

In solution, substrates **1**–**4** were converted with catalysts **W1** and **W2** into the corresponding macrocycles in 71–74% yield. MC efficiency was in the range of 27–48%; the *Z*-content was in the range of 17–37%. With the supported catalysts **W1@OMS** and **W2@OMS** conversions were in the range of 27–53% and thus lower than in solution; hindered diffusion can be made accountable for that. Most important, MC selectivity increased substantially upon immobilization of **W1** or **W2** inside the mesopores of OMS. For substrate **1**, whose MC yields the

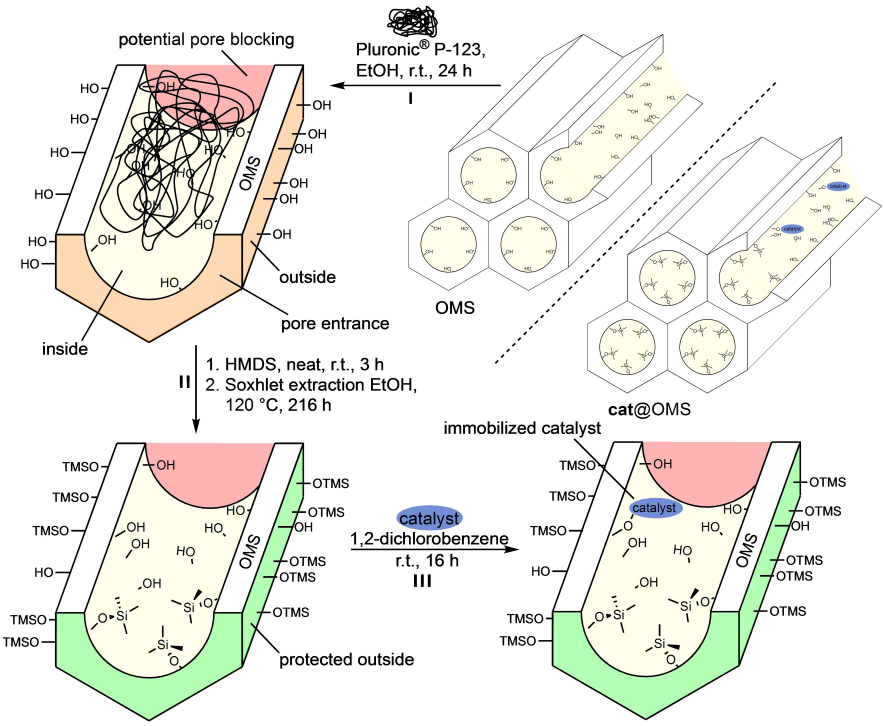

Figure 2. Multi-step modification of OMS for the pore-selective immobilization of the catalyst inside the mesopores.

20-membered ring **5**, MC selectivity increased from 48% (**W1**, **W2**) to 80% (**W1@OMS$_{68Å}$**) using 6.8 nm pores and could be further increased to 86% (**W1@OMS$_{33Å}$**) using 3.3 nm pores.

Remarkably, the use of the double amount of catalyst (2 mol-%) did not change MC selectivity significantly but increased the conversion notably (Table 1). *Z*-selectivity increased substantially from 37% (**W1**) to 59% (**W1@OMS$_{33Å}$**). For substrate **2**, whose MC yields the 27-membered ring **6**, MC selectivity increased from 45% (**W1**) to 71% (**W1@OMS$_{68Å}$**) using 6.8 nm pores and could be further increased to 78% (**W1@OMS$_{33Å}$**) using 3.3 nm pores. Again, the use of the double amount of catalyst (2 mol-%) did not significantly change MC selectivity. *Z*-selectivity also increased from 24% (**W2**) to 41% (**W2@OMS$_{33Å}$**). Substrate **3**, yielding the largest macrocycle **7**, i.e. a 34-membered ring, showed similar results. MC selectivity increased from 37% (**W1**) to 61% (**W1@OMS$_{68Å}$**) using 6.8 nm pores and further increased to 70% (**W1@OMS$_{33Å}$**) using 3.3 nm pores. Due to overlapping signals in ^{1}H NMR, *Z*-selectivity could not be accurately determined. Finally, the MC selectivity of substrate **4**, yielding the 17-membered ring **8**, was successfully increased from 27% (**W1**) to 72% (**W1@OMS$_{68Å}$**) using 6.8 nm pores and to 81% (**W1@OMS$_{33Å}$**) using 3.3 nm pores. *Z*-selectivity also increased from 22% (**W2**) to 40% (**W2@OMS$_{33Å}$**).

EXAFS Analysis

Tungsten L_3 XANES spectra of **W1** and **W1@OMS$_{68Å}$** in comparison to a tungsten foil are shown in Figure 3 together with their 1st derivatives in the inset. The absorption edge shift by +1.5 eV after immobilization indicates a significant change of the electronic structure in **W1@OMS$_{68Å}$**. It has to be noticed that this shift is not necessarily indicating an oxidation state change. In fact, since the white line intensity is identical in both **W1** and **W1@OMS$_{68Å}$**, identical oxidation states can be assumed, as it reflects the number of d-electron holes.[11] EXAFS analysis was performed to determine the local structure of **W1** and **W1@OMS$_{68Å}$**. As shown in Table 2, the first coordination shell is composed of five atoms according to the structural model of **W1**. To account for oscillation anharmonicity, the first shell scatters were fitted with the third cumulant.[12] Concerning atom types, EXAFS cannot distinguish between them due to almost identical scattering factors and phase shifts. Thus, the first double-degenerated W–C scatter at 1.818(9) Å contains contributions from N and C atoms. Likewise, the third double-degenerated W–C scatter at 2.200(4) Å also contains contributions from C and N atoms. The fitting details on further coordination shells are available in Table S9 and the fits are shown in Figure S34.

Compared to **W1**, the coordination environment in **W1@OMS$_{68Å}$** changes significantly. Upon immobilization, decoordination of the nitrile and a 4-fold coordination is expected. To create a suitable model for the fit of the according EXAFS spectrum, the structure of **W1** was modified accordingly followed by geometry optimization using DFT calculations (Orca 5.0.2 version)[13] with the PBEh-3c method[14] and fixed positions of the Si atoms. The final XYZ coordinates of the optimized structure are provided in Table S11. Results concerning the 1st coordination shell for EXAFS analysis based on this model are shown in Table 3, while the further shell data is

Table 1. Summary of macrocyclization (MC) results.

Substrate	Catalyst	Conversion [%]	MC-Selectivity [%]	% *Z*
1	W1	72	48	37
1	W1@OMS$_{68Å}$	27	80	53
1	W1@OMS$_{68Å}$[a]	51	82	50
1	W1@OMS$_{33Å}$	31	86	58
1	W1@OMS$_{33Å}$[a]	42	86	53
1	W2	74	48	36
1	W2@OMS$_{33Å}$	44	70	50
1	W2@OMS$_{33Å}$	40	84	59
2	W1	71	45	26
2	W1@OMS$_{68Å}$	31	71	32
2	W1@OMS$_{68Å}$[a]	53	69	33
2	W1@OMS$_{33Å}$	44	78	35
2	W1@OMS$_{33Å}$[a]	40	78	37
2	W2	73	46	24
2	W2@OMS$_{68Å}$	50	62	35
2	W2@OMS$_{33Å}$	37	72	41
3	W1	71	37	–
3	W1@OMS$_{68Å}$	18	61	–
3	W1@OMS$_{33Å}$	14	70	–
3	W2	74	38	–
3	W2@OMS$_{68Å}$	43	54	–
3	W2@OMS$_{33Å}$	30	65	–
4	W1	71	27	17
4	W1@OMS$_{68Å}$	33	72	30
4	W1@OMS$_{33Å}$	26	81	34
4	W2	72	29	22
4	W2@OMS$_{68Å}$	49	53	32
4	W2@OMS$_{33Å}$	30	70	40

Reactions were run at room temperature in C_6D_6 for 16 hours using 1 mol-% catalyst and a substrate concentration of 25 mM. [a]2 mol-% catalyst.

Table 2. W L_3 EXAFS results for W1.

Path	N	σ^2/Å^2	R_{eff}/Å	R + ΔR/Å	C_3/Å^3
W–C/N	1.8(1)	0.0021(2)	1.872	1.818(9)	0.00027(10)
W-O	1.4(1)	0.0035(5)	1.996	1.937(6)	0
W–C/N	2.1(1)	0.0024(2)	2.186	2.200(4)	0.00027(10)

N – coordination number; σ^2 – Debye–Waller factor; R_{eff} – model values; R + ΔR – fitted positions; C_3 – third cumulant. The values in brackets indicate a fitting error at a 0.95 confidence level.

available in Table S10 and fitted function in Figure S35. The generated model with the 4-fold coordination environment reproduces the experimental spectra very well. Two double-degenerated scatters indicate a higher symmetry than in **W1**. Thus, the W–C scatter at 1.79 Å contains contributions from C and N atoms. The second W–O double-degenerated scatter contains contributions from W–O and W–C. The original W–C

Table 3. W L_3 EXAFS results for W1@OMS$_{68Å}$.

Path	N	σ^2/Å^2	R_{eff}/Å	R + ΔR/Å	C_3/Å^3
W–C/N	1.8(1)	0.0020(3)	1.891	1.794(13)	0.00051(14)
W–O/C	1.8(1)	0.0026(3)	1.897	1.898(14)	−0.00069(14)

N – coordination number; σ^2 – Debye–Waller factor; R_{eff} – model values; R + ΔR – fitted positions; C_3 – third cumulant. The values in brackets indicate a fitting error at a 0.95 confidence level.

bond with the 1,3-dimesitylimidazol-2-ylidene group at 2.20 Å in **W1**, is significantly shorter in **W1@OMS$_{68Å}$** (1.90 Å), which contracts a major part of the complex. Interestingly, at 3.75 Å, a W–Si backscatter pair is visible, which is affected by strong anharmonicity of oscillations, a row of magnitude higher than for W–C and W–O oscillations. It can be rationalized by strong movement constraints on the Si atom due to the rigid support type.

Discussion

All reactions were run 25 mM in substrate, which is substantially higher than the usual 5 mM up to which MC reactions are usually run to achieve high MC selectivity. In solution, **W1** and **W2** performed almost identical for a given substrate in terms of conversion and MC selectivity and showed only subtle differences in *Z*-selectivity. Yields were only slightly lower than with related cationic Mo imido alkylidene NHC catalysts ($\leq$74 vs. $\leq$79 %).[5b] Under confinement, both supported catalysts **W1@OMS** and **W2@OMS** allowed for substantially higher MC selectivity and *Z*-selectivity compared to the homogeneous analogs **W1** or **W2**, particularly when immobilized inside small 3.3 nm mesopores. Moreover, particularly for the least polar substrate **4**, the supported catalyst **W1@OMS$_{33Å}$** allowed for a higher MC selectivity than **W2@OMS$_{33Å}$**, which can be rationalized by the more non-polar environment around the catalyst resulting from the presence of the 2,6-dichlorophenylimido ligand compared to the oxo ligand. By contrast, **W2@OMS$_{33Å}$** allowed for a systematically and significantly higher *Z*-selectivity than **W1@OMS$_{33Å}$**. This is a direct result of the oxo-moiety in **W2**, which favors the *Z*-tungstacyclobutane transition state more than the imido-bearing **W1** (Figure 4), at least in a trigonal-bipyramidal configure transition state. However, it should be stated that cationic tungsten alkylidene NHC catalysts can also adopt square pyramidal transition states, in which the above-discussed effects become less effective.

Compared to the analogous supported cationic molybdenum imido alkylidene NHC complex [Mo(N-2,6-Me_2-C_6H_3)(CHCMe_2Ph)(IMes)(≡SiO)$^+$ $B(Ar^F)_4^-$],[5b] both **W1@OMS** and **W2@OMS** give very similar results in terms of MC selectivity. This is in line with earlier studies, which revealed that the corresponding ring-chain equilibria are reached at an early stage of the reaction, i.e. around 2% conversion.[5c] Consequently, MC selectivity must be independent of the catalyst used, provided no additional parameters such as different

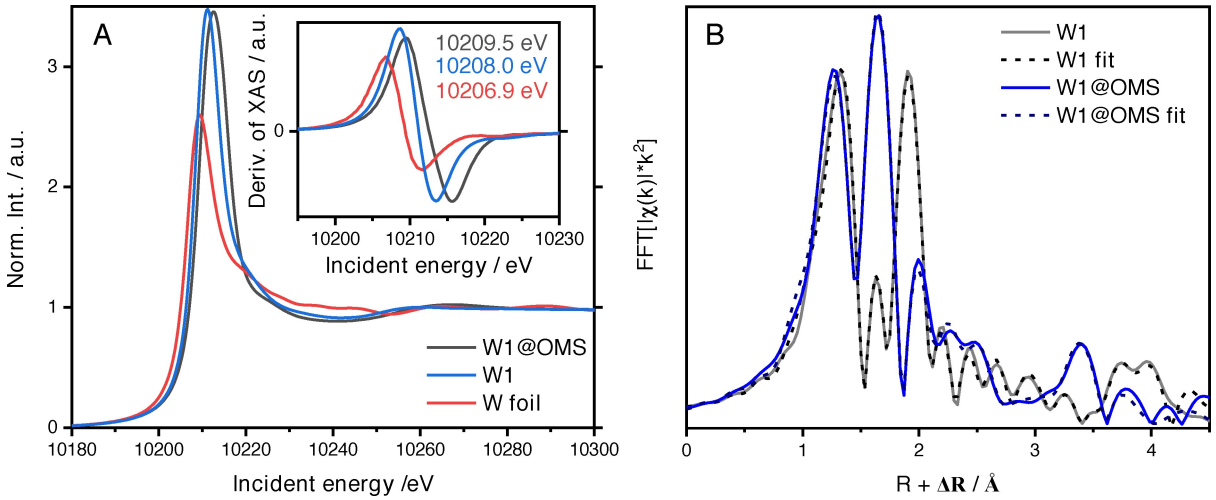

Figure 3. A) Tungsten L_3 XANES spectra of W1 and W1@$OMS_{68Å}$ in comparison to a W foil. Insert shows corresponding 1st derivatives of spectra; B) Fourier-transformed EXAFS along with fitted models for W1 (grey/black) and W1@$OMS_{68Å}$ (blue/dark blue).

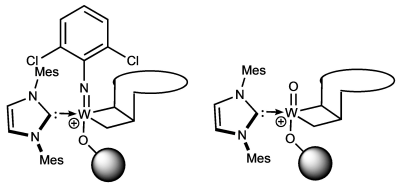

Figure 4. Structures of *Z*-tungstacyclobutane transition states responsible for high *Z*-selectivity derived from W1 and W2, respectively.

distance to the pore wall or polarity become effective. By contrast, compared to the analogous supported cationic molybdenum imido alkylidene NHC complex [Mo(N-2,6-Me_2-C_6H_3)(CHCMe$_2$Ph)(IMes)(≡SiO)$^+$ B(Ar^F)$_4^-$],[5b] *Z*-selectivity is slightly higher with both, **W1@OMS** and **W2@OMS**. The maximum *Z*-selectivity for substrates **1**, **2** and **4** was 59%, 41% and 40% with the W-based systems compared to 46%, 34% and 38% with the Mo-catalysts.[5b] Whether this higher *Z*-selectivity is a result of a more contracted structure as found by XAS (*vide supra*), resulting in a more constraint geometry around the metal center, remains a likely but speculative explanation. MC selectivity did not substantially change with conversion for both **W1@OMS$_{33Å}$** and **W1@OMS$_{68Å}$** and showed only a minor drop from 90% to 86% and from 83% to 80% over time (Tables S4, S5, Supporting Information), as exemplified for substrate **1**. In line with these findings, the reactivity of the **W1** system was found to be comparable to the one of the supported Mo-based [Mo(N-2,6-Me_2-C_6H_3)(CHCMe$_2$Ph)(IMes)(≡SiO)$^+$ B(Ar^F)$_4^-$] catalyst.[5b] Thus, the values for the initial turnover frequency ($TOF_{30\ min}$) of **W1@OMS$_{68\ Å}$** and **W1@OMS$_{33\ Å}$** in C_6D_6 at room temperature for substrate **1** were 0.45 min^{-1} and 0.38 min^{-1} (Figure S33), respectively, while those for the corresponding Mo-complexes were 0.49 min^{-1}, 0.26 min^{-1}, respectively.[15]

Conclusions

A cationic tungsten oxo alkylidene NHC and a cationic tungsten imido alkylidene NHC catalyst have successfully been immobilized inside the pores of two different mesoporous silica materials using a pore-selective immobilization protocol. The structure of the supported cationic tungsten imido alkylidene NHC catalyst was confirmed by XAS. Both catalysts allow for the selective macrocyclization of various α,ω-dienes with high macrocyclization efficiency and appreciable *Z*-selectivity, substantially exceeding the homogenous analogues. Macrocyclization and *Z*-selectivity are highest with the smallest pores. The results presented here are in line with those obtained previously both in the macrocyclization and ring-opening cross-metathesis (ROCM)[6] with cationic molybdenum imido alkylidene NHC complexes under confinement and illustrate the generality of the confinement approach outlined here.

Experimental

General: All reactions were performed under the exclusion of air and moisture in a N_2-filled glove box (MBraun Labmaster) unless noted otherwise. Chemicals were purchased from ABCR, Acros Organics, Alfa Aesar, Sigma Aldrich, Fluka and TCI. Poly(ethylene glycol)-*b*-poly(propylene glycol)-*b*-poly(ethylene glycol) (PEG-PPG-PEG, Pluronic® P-123), dodecylethyldimethylammonium bromide (≥ 98%), tetramethyl orthosilicate (98%, TMOS) and 1,2-dichlorobenzene (anhydrous) were purchased from Sigma Aldrich. CH_2Cl_2, diethyl ether, *n*-pentane and toluene were dried using an MBraun SPS-800 solvent purification system and stored over 4 Å molecular sieves. Deuterated solvents were stored over activated alumina and 4 Å molecular sieves for a minimum of 24 h prior to use. NMR spectra were recorded on a Bruker Avance III 400 spectrometer at 400 MHz for proton and at 101 MHz for carbon. NMR spectra were internally calibrated to solvent signals.[16] Abbreviations for multiplicities: s (singlet), bs (broad singlet), d (dublet), t (triplet), q (quartet), hept (heptet), m (multiplet). Elemental analyses were measured on a Perkin Elmer 240 device at the Institute of Inorganic Chemistry, University of Stuttgart, Germany. High performance

liquid chromatography (HPLC) was performed at the Institute of Organic Chemistry, University of Stuttgart, Germany using a Knauer K-501 pump, a Knauer K 2400 RI-detector and a Macherey & Nagel VP250/21 Nucleodur 100–5 column. Argon and nitrogen adsorption analyses were performed at 87 K and 77 K, respectively, on a Quantachrome Autosorb iQ MP automatic volumetric instrument (for Argon) Quantachrome QuadraSorb automatic volumetric instrument (for nitrogen). Silica samples were degassed for 11 h at 150 °C under vacuum prior to the gas adsorption studies. Pore size distributions, pore volumes and surface areas were calculated from the desorption branch using the non-local Density Functional Theory (NLDFT) cylindrical adsorption pores for zeolites/silica implemented in the ASiQwin software version 3.01. Small-angle X-ray scattering (SAXS) experiments were performed at 25 °C with an Anton Paar SAXSess mc^2 equipped with a Dectris Mythen 1 K detector. Cu–Kα radiation was generated with an ID 3003 X-ray generator (Seifert) operated at 40 kV and 40 mA and line collimated. Deconvolution of the measured SAXS curves was performed with the software SAXSquant (Anton Paar). The sample to detector distance was calibrated using a sample of powdered cholesteryl palmitate. ICP-OES data were recorded on a Spectro Acros 160 CCD equipped with a Cetec ASX-260 autosampler. Analysis of the samples was carried out with the Software Smart Analyzer Vision 4.02.0834. Scanning electron microscopy (SEM) analysis was performed at the AMICA core facility of the University of Stuttgart. After sputtering with gold, samples were measured with a Zeiss Evo 15 using a secondary electron detector and the associated software SmartSEM 6.07 (Zeiss).

IMes,[17] **W1**,[8] **W2**[7h] and (*E*)+(*Z*)-cycloheptadec-9-en-1-ol,[18] dec-9-en-1-yl undec-10-enoate **1**,[5b,d,10] pentane-1,5-diyl bis(undec-10-enoate),[5b,d,10] dodecane-1,12-diyl bis(undec-10-enoate) **3**,[5d] tert-butyldimethyl(nonadeca-1,18-dien-10-yloxy)silane **4**[5b,10] were synthesized according to the literature.

Determination of the metal loading via ICP-OES: Quantitative analysis of the W-loading of each silica sample was determined by ICP-OES. For analysis, the corresponding silica (30-50 mg, Table S2) was mixed with KOH (0.38 g, 6.77 mmol) and KNO_3 (0.65 g, 6.42 mmol). The mixture was heated to 450 °C and the temperature was held for 3 hours. After cooling to room temperature, $K_2S_2O_8$ (50.0 mg, 0.18 mmol) was added. The colorless solid was dissolved in a minimum amount of deionized water and 1 M KOH (2 mL) was added. The suspension was filtered, transferred into a 10 mL volumetric flask and filled to the mark with deionized water. The solution was slowly added to a 25 mL volumetric flask with concentrated HCl (5 mL) and filled to the mark with deionized water. This solution was analyzed by ICP-OES for W. W was measured at λ = 207.911 nm; the background was measured at λ = 207.84 nm–207.87 nm and λ = 207.99 nm–208.04 nm, respectively. The limit of detection (LOD) was 0.0001 mg. L^{-1}. For calibration, aqueous W-standards with W concentration of 0.000, 0.100, 0.500, 1.000, 2.500 and 5.000 mg L^{-1} were used. A reference, containing the same amount of KOH, KNO_3, HCl and deionized water was subjected to the same treatment for comparison.

General Procedure for the RCM of α,ω-Dienes (GP-1): To a stirred solution of the diene (0.75 mmol) in CH_2Cl_2 (200 mL) was added the 2nd-generation Grubbs catalyst $RuCl_2$(IMes)(PCy_3)(CHPh) (31.8 mg, 0.0375 mmol, 5 mol-%) at room temperature. After stirring for 14 hours under reflux and under N_2, the reaction mixture was cooled to room temperature and ethyl vinyl ether (5 mL, 70 eq) was added. The mixture was stirred for a further 2 hours at room temperature. All volatiles were removed under reduced pressure and the obtained crude product was purified via column chromatography on SiO_2 to obtain the corresponding macrocyclic product, whose *E/Z* isomers were separated by semi-preparative HPLC.

(E)-Oxacycloicos-11-en-2-one ((E)-5): The compound was prepared according to GP-1. The α,ω-diene **1** (241.9 mg, 0.75 mmol) was dissolved in CH_2Cl_2 (250 mL), treated with the 2nd-generation Grubbs catalyst (31.8 mg, 0.0375 mmol, 5 mol%) to yield the corresponding macrocycle ***E*-5** after column chromatography over SiO_2 and semi-preparative HPLC (petroleum ether:ethyl acetate–75:1) as colorless liquid. Spectral data were in good agreement with previous reports.[5d,10] ^{1}H NMR (C_6D_6) δ 5.31–5.41 (m, 2H), 4.00–4.05 (m, 2H), 2.15 (t, J = 6.6 Hz, 2H), 1.99–2.07 (m, 4H), 1.54–1.61 (m, 2H), 1.38–1.44 (m, 2H), 1.18–1.37 (m, 20H) ppm; ^{13}C NMR (C_6D_6) δ 173.0, 131.1, 131.0, 64.0, 34.0, 32.3, 32.2, 29.7, 29.5, 29.3, 29.2, 29.1, 29.0, 28.9, 28.5, 28.0, 27.9, 26.4, 25.2 ppm; IR (ATR, in C_6D_6): 2922 (s), 2852 (m), 1734 (s), 1460 (w), 1440 (w), 1387 (w), 1348 (w), 1253 (m), 1236 (m), 1172 (m), 1119 (m), 1098 (m), 1061 (w), 1022 (w), 966 (m) cm^{-1}.

(Z)-Oxacycloicos-11-en-2-one ((Z)-5): The compound was prepared according to GP-1. The α,ω-diene **1** (241.9 mg, 0.75 mmol) was dissolved in CH_2Cl_2 (250 mL), treated with the 2nd-generation Grubbs catalyst (31.8 mg, 0.0375 mmol, 5 mol%) to yield the corresponding macrocycle ***Z*-5** after column chromatography over SiO_2 and semi-preparative HPLC (petroleum ether:ethyl acetate–75:1). Spectral data were in good agreement with previous reports.[5d,10] ^{1}H NMR (C_6D_6) δ 5.40–5.50 (m, 2H), 4.05 (t, J = 5.7 Hz, 2H), 2.17 (t, J = 6.8 Hz, 2H), 2.02–2.09 (m, 4H), 1.51–1.58 (m, 2H), 1.32–1.43 (m, 6H), 1.20–1.30 (m, 16H) ppm; ^{13}C NMR (C_6D_6) δ 172.9, 130.4, 130.3, 64.0, 34.8, 29.7, 29.6, 29.4, 29.2, 29.2, 29.1, 29.0, 28.9, 28.8, 28.5, 26.9, 26.8, 26.6, 25.5 ppm; IR (ATR, in C_6D_6): 3002 (w), 2923 (s), 2853 (m), 1734 (s), 1461 (w), 1385 (w), 1345 (w), 1237 (m), 1173 (m), 1116 (w), 1093 (w), 1065 (w), 1018 (w) cm^{-1}.

E/Z-1,7-Dioxacycloheptacos-17-ene-8,27-dione (E/Z-6): The compound was prepared following GP-1. The α,ω-diene 4 (327.5 mg, 0.75 mmol) was dissolved in CH_2Cl_2 (250 mL) and treated with the 2nd-generation Grubbs catalyst (31.8 mg, 0.0375 mmol, 5 mol%) to yield the corresponding macrocycle ***E/Z*-6** as white solid after column chromatography over SiO_2 as an inseparable mixture. Spectral data were in good agreement with previous reports.[5d,19] ^{1}H NMR (C_6D_6) δ 5.44–5.49 (m, 0.38H), 5.40–5.43 (m, 1.62H), 3.99 (t, J = 5.7 Hz, 4H), 2.18 (t, J = 7.3 Hz, 0.76H), 2.17 (t, J = 7.4 Hz, 3.24H), 2.03–2.10 (m, 4H), 1.56–1.62 (m, 4H), 1.19–1.39 (m, 26H) ppm; ^{13}C NMR (C_6D_6) δ 173.0, 173.0, 131.0, 130.4, 63.9, 63.8, 34.5, 32.7, 29.8, 29.5, 29.4, 29.4, 29.3, 29.2, 29.1, 28.7, 28.6, 27.3, 25.4, 23.2, 23.1 ppm. Five carbons were not observed due to incidental equivalence; IR (ATR, in C_6D_6): 2923 (s), 2853 (m), 1734 (s), 1457 (w), 1441 (w), 1420 (w), 1388 (w), 1357 (w), 1238 (m), 1173 (m), 1112 (w), 1094 (w), 1047 (w), 968 (w) cm^{-1}; HRMS (EI, *m/z*) calcd. for $C_{25}H_{44}O_4^+$: 408.3240; found: 408.3238.

(E/Z)-1,14-Dioxacyclotetratriacont-24-ene-15,34-dione (E/Z-7): The compound was prepared according to GP-1. The α,ω-diene 3 (401.1 mg, 0.75 mmol) was dissolved in CH_2Cl_2 (250 mL), treated with the 2nd-generation Grubbs catalyst (31.8 mg, 0.0375 mmol, 5 mol%) to yield the corresponding (*E/Z*)-macrocycle after column chromatography on SiO_2 as an inseparable mixture in form of a colorless crystalline solid. ^{1}H NMR (C_6D_6) δ 5.36–5.45 (m, 2H), 4.02 (t, J = 6.3 Hz, 4H), 2.16 (t, J = 7.2 Hz, 3.45H), 2.15 (t, J = 7.2 Hz, 0.55H), 1.95–2.05 (m, 4H), 1.52–1.57 (m, 4H), 1.42–1.49 (m, 4H), 1.28–1.35 (m, 4H), 1.13–1.28 (m, 32H) ppm. ^{13}C NMR (C_6D_6) δ 172.9, 130.7, 130.2, 64.1, 34.5, 34.5, 33.0, 30.1, 29.8, 29.8, 29.7, 29.7, 29.6, 29.5, 29.5, 29.4, 29.4, 29.3, 29.2, 29.1, 29.1, 27.6, 26.4, 26.3, 25.4 ppm. IR (ATR, in C_6D_6): 2915 (s), 2849 (m), 1727 (s), 1468 (m), 1434 (w), 1379 (w), 1335 (w), 1323 (w), 1304 (w), 1249 (m), 1208 (w), 1161 (m), 1150 (m), 1113 (w), 1088 (w), 1065 (w), 1034 (w) cm^{-1}. HRMS (ESI, *m/z*) calcd. for $C_{32}H_{58}O_4Na^+$: 529.4227, found: 529.4223.

(E/Z)-tert-Butyl(cycloheptadec-9-en-1-yloxy)dimethylsilane (E/Z-8): To a solution of *E/Z*-cycloheptadec-9-en-1-ol (12.6 mg, 0.05 mmol) in

DMF (1 mL) were subsequently added imidazole (10.2 mg, 0.15 mmol) and *tert*-butyldimethylsilyl chloride (11.3 mg, 0.075 mmol). After stirring overnight at room temperature, ethanol (1 mL) was added and the reaction mixture was stirred for a further 15 minutes. The mixture was then diluted with n-pentane (10 mL), washed with H_2O (15 mL) and brine (15 mL), dried over anhydrous Na_2SO_4, filtered and all volatiles were removed *in vacuo*. The obtained crude product was purified by column chromatography over SiO_2 (*n*-pentane:diethyl ether–100:0→100:1) to yield the corresponding macrocycle ***E/Z*-8** as an inseparable mixture on form of a colorless oil. Spectral data were in agreement with previous reports.[5d,10] ^{1}H NMR (C_6D_6) δ 5.39–5.43 (m, 0.21H), 5.31–5.37 (m, 1.79H), 3.75–3.81 (m, 1H), 2.00–2.10 (m, 4H), 1.50–1.63 (m, 4H), 1.26–1.43 (m, 20H), 1.03 (s, 9H), 0.12 (s, 6H) ppm; ^{13}C NMR (C_6D_6) δ 131.1, 130.4, 72.1, 71.6, 36.3, 36.1, 32.8, 29.5, 29.4, 29.2, 29.0, 28.5, 28.5, 28.2, 27.6, 27.3, 26.2, 23.8, 22.9, 18.4, −4.3, −4.4 ppm. Two carbons were not observed due to incidental equivalence; IR (ATR in C_6D_6): 3026 (w), 2925 (s), 2854 (s), 1472 (w), 1461 (w), 1443 (w), 1405 (w), 1388 (w), 1373 (w), 1360 (w), 1254 (m), 1211 (w), 1188 (w), 1101 (w), 1050 (m), 1005 (w), 966 (m) cm^{-1}.

Synthesis of Ordered Mesoporous Silica ($OMS_{33Å}$, $OMS_{68Å}$): OMS materials were synthesized via a true liquid crystal templating process as described previously.[5b,20] In brief, for the synthesis of $OMS_{33Å}$ 38 g of TMOS were added to 27 g of 0.1 N HCl in a polypropylene flask. The forming methanol was removed by rotary evaporation for 15 minutes at 40 °C and 280 mbar. The mixture was then added to 18 g of cetyldiethylammonium bromide and stirred with a KPG-stirrer until a homogenous, clear solution was obtained. For the synthesis of $OMS_{68Å}$ 30.4 g of TMOS were added to 21.6 g of 0.1 N HCl in a polypropylene flask. The forming methanol was removed as described before. Subsequently, the mixture was added to 17.7 g of P123 and 1 g of hexadecane and stirred until homogenous. The two obtained clear solutions were poured into PTFA dishes and cured for two to three days at 80 °C. The now solid materials were milled for 1 min with a ball mill (Spex 8000 Mixer/Mill, vial and balls made from stainless steel). Afterwards, the powder materials were calcined by heating them to 550 °C with 1 °C·min^{-1} and keeping them at this temperature for 6 h to remove all surfactant molecules. An airflow of 14.5 L·h^{-1} was applied during calcination.

EXAFS measurements

W L_3 Extended X-Ray Absorption Fine Structure measurement were conducted at the P65 beamline, Petra III, DESY (Hamburg).[21] Energy selection was done with a Si(111) double crystal monochromator; the energy resolution was around 1.0 eV at 10 keV. The beam spot size was 0.3 x 1 mm^2 and the total flux on the sample was 10^{12} ph/s. Signal detection was conducted in the fluorescence mode using a PIPS detector, all at room temperature. For beam focusing and higher harmonic rejections, Rh-coated mirrors were used. Data acquisition was performed in the continuous scanning mode and spectra were rebinned afterwards. Energy calibration was conducted at the first inflection point of the pure W XANES spectrum (10206.9 eV). To avoid radiation damage, each EXAFS spectrum was collected at a different sample position. Initial normalization and background removal were conducted with the Athena software;[22] EXAFS fitting was performed with the Artemis package[22] using the Multiple Scattering approach. The analysis was conducted in the k-range of 2.0–15.0 Å^{-1} and real space of 1.0–4.2 Å.

Contributions

MRB elaborated the concepts and wrote the manuscript. FZ carried out all immobilizations, catalyst synthesis and macrocyclization experiments. JRB provided the OMS materials. PP helped in analyzing the data and recorded the reaction kinetics. MN and MB contributed the XAS data, BA and JRB recorded and interpreted the gas sorption experiments.

Supporting Information

Additional information concerning the characterization of the OMS as well as their modification, the macrocyclization reactions, ^{1}H-NMR and EXAFS spectra are available online. Primary data is accessible via the following link: https://doi.org/10.18419/darus-3702. The authors have cited additional references within the Supporting Information.[23]

Acknowledgements

Financial support provided by Deutsche Forschungsgemeinschaft DFG (German Research Foundation, project ID 358283783 – CRC 1333/2 2022 and AOBJ: 642944) and the European Regional Development Fund (EFRE, FEIH 778511) is gratefully acknowledged. This project was also supported by the Ministry of Science, Research and the Arts Baden-Württemberg. We also acknowledge DESY (Hamburg, Germany), a member of the Helmholtz Association HGF, for the provision of experimental facilities. Parts of this research were carried out at Petra III. We thank Dr. Edmund Welter for assistance in using the P65 beamline. Beamtime was allocated for proposal I-20220206. We gratefully acknowledge the core facility SRF AMICA (Stuttgart Research Focus Advanced Materials Innovation and Characterization) at the University of Stuttgart for their support and assistance in this work. Open Access funding enabled and organized by Projekt DEAL.

Conflict of Interests

The authors declare no conflict of interest.

Data Availability Statement

The data that support the findings of this study are available from the corresponding author upon reasonable request.

Keywords: tungsten · *N*-heterocyclic carbene · macrocyclization · confinement

[1] K. Wang, J. H. Jordan, X.-Y. Hu, L. Wang, *Angew. Chem. Int. Ed.* **2020**, *132*, 13816–13825.
[2] a) T. M. Bräuer, Q. Zhang, K. Tiefenbacher, *Angew. Chem. Int. Ed.* **2016**, *128*, 7829–7832; b) T. M. Bräuer, Q. Zhang, K. Tiefenbacher, *J. Am. Chem.*

Soc. **2017**, *139*, 17500–17507; c) C. Bianchini, D. G. Burnaby, J. Evans, P. Frediani, A. Meli, W. Oberhauser, R. Psaro, L. Sordelli, F. Vizza, *J. Am. Chem. Soc.* **1999**, *121*, 5961–5971; d) F. Zhang, C. Kang, Y. Wei, H. Li, *Adv. Funct. Mater.* **2011**, *21*, 3189–3197; e) S. A. Raynor, J. M. Thomas, R. Raja, B. F. G. Johnson, R. G. Bell, M. D. Mantle, *Chem. Commun.* **2000**, 1925–1926.

[3] C. Zhao, F. D. Toste, K. N. Raymond, R. G. Bergman, *J. Am. Chem. Soc.* **2014**, *136*, 14409–14412.

[4] a) S.-G. Shyu, S.-W. Cheng, D.-L. Tzou, *Chem. Commun.* **1999**, 2337–2338; b) P. Piaggio, P. McMorn, C. Langham, D. Bethell, P. C. Bulman-Page, F. E. Hancock, G. J. Hutchings, *New J. Chem.* **1998**, *22*, 1167–1169.

[5] a) S. T. Emmerling, F. Ziegler, F. R. Fischer, R. Schoch, M. Bauer, B. Plietker, M. R. Buchmeiser, B. V. Lotsch, *Chem. Eur. J.* **2022**, *28*, e202104108; b) F. Ziegler, H. Kraus, M. J. Benedikter, D. Wang, J. R. Bruckner, M. Nowakowski, K. Weißer, H. Solodenko, G. Schmitz, M. Bauer, N. Hansen, M. R. Buchmeiser, *ACS Catal.* **2021**, *11*, 11570–11578; c) F. Ziegler, M. Pyschik, T. Roider, C. P. Haas, D. Wang, U. Tallarek, M. R. Buchmeiser, *ChemCatChem* **2021**, *13*, 2234–2241; d) F. Ziegler, J. Teske, I. Elser, M. Dyballa, W. Frey, H. Kraus, N. Hansen, J. Rybka, U. Tallarek, M. R. Buchmeiser, *J. Am. Chem. Soc.* **2019**, *141*, 19014–19022; e) P. K. R. Panyam, B. Atwi, F. Ziegler, W. Frey, M. Nowakowski, M. Bauer, M. R. Buchmeiser, *Chem. Eur. J.* **2021**, *27*, 17220–17229; f) P. K. R. Panyam, M. R. Buchmeiser, *Faraday Discuss.* **2023**, *in press*, 10.1039/D1032FD00152G; g) A. Böth, T. Roider, F. Ziegler, X. Xie, M. R. Buchmeiser, U. Tallarek, *ChemCatChem* **2022**, *15*, e202201268; h) U. Tallarek, J. Hochstrasser, F. Ziegler, X. Huang, C. Kübel, M. R. Buchmeiser, *ChemCatChem* **2021**, *13*, 281–292.

[6] E. L. Goldstein, F. Ziegler, J. R. Bruckner, A.-K. Beurer, Y. Traa, M. R. Buchmeiser, *ChemCatChem* **2022**, *14*, e202201008.

[7] a) M. R. Buchmeiser, *Chem. Eur. J.* **2018**, *24*, 14295–14301; b) J. De Jesus Silva, D. Mance, M. Pucino, M. J. Benedikter, I. Elser, M. R. Buchmeiser, C. Copéret, *Helv. Chim. Acta (special issue in dedication of Prof. Togni's retirement)* **2020**, *103*, e2000161; c) I. Elser, J. Groos, P. M. Hauser, M. Koy, M. van der Ende, W. Frey, K. Wurst, J. Meisner, J. Kästner, M. R. Buchmeiser, *Organometallics* **2019**, *38*, 4133–4146; d) I. Elser, R. Schowner, W. Frey, M. R. Buchmeiser, *Chem. Eur. J.* **2017**, *23*, 6398–6405; e) P. M. Hauser, M. van der Ende, J. Groos, W. Frey, D. Wang, M. R. Buchmeiser, *Eur. J. Inorg. Chem.* **2020**, *2020*, 3070–3082; f) J. V. Musso, P. Gebel, V. Gramm, W. Frey, M. R. Buchmeiser, *Macromolecules* **2023**, *56*, 2878–2888; g) M. Pucino, V. Mougel, R. Schowner, A. Fedorov, M. R. Buchmeiser, C. Copéret, *Angew. Chem. Int. Ed.* **2016**, *128*, 4372–4374; h) R. Schowner, W. Frey, M. R. Buchmeiser, *J. Am. Chem. Soc.* **2015**, *137*, 6188–6191; i) R. Schowner, J. V. Musso, W. Frey, M. R. Buchmeiser, *Organometallics* **2021**, *40*, 3145–3157; j) M. J. Benedikter, F. Ziegler, J. Groos, P. M. Hauser, R. Schowner, M. R. Buchmeiser, *Coord. Chem. Rev.* **2020**, *415*, 213315; k) R. R. Schrock, M. R. Buchmeiser, J. Groos, M. J. Benedikter, *Comprehensive Organometallic Chemistry IV (4th Ed.)* **2022**, *5*, 671–773.

[8] J. V. Musso, M. Benedikter, P. Gebel, V. Gramm, D. Wang, R. Schowner, M. R. Buchmeiser, *Polym. Chem.* **2021**, *12*, 5979–5985.

[9] a) D. C. Martínez Casillas, M. P. Longinotti, M. M. Bruno, F. Vaca Chávez, R. H. Acosta, H. R. Corti, *J. Phys. Chem. C* **2018**, *122*, 3638–3647; b) V. T. Hoang, Q. Huang, M. Eic, T. O. Do, S. Kaliaguine, *Langmuir* **2005**, *21*, 2051–2057.

[10] V. M. Marx, M. B. Herbert, B. K. Keitz, R. H. Grubbs, *J. Am. Chem. Soc.* **2013**, *135*, 94–97.

[11] S. Preiß, C. Förster, S. Otto, M. Bauer, P. Müller, D. Hinderberger, H. H. Haeri, L. Carella, K. Heinze, *Nat. Chem.* **2017**, *9*, 1249–1255.

[12] M. Bauer, H. Bertagnolli, *J. Phys. Chem. B* **2007**, *111*, 13756–13764.

[13] F. Neese, *WIREs Comput. Mol. Sci.* **2012**, *2*, 73–78.

[14] S. Grimme, J. G. Brandenburg, C. Bannwarth, A. Hansen, *J. Chem. Phys.* **2015**, *143*, 054107.

[15] F. Ziegler, H. Kraus, M. J. Benedikter, D. Wang, J. R. Bruckner, M. Nowakowski, K. Weißer, H. Solodenko, G. Schmitz, M. Bauer, N. Hansen, M. R. Buchmeiser, *ACS Catal.* **2021**, *11*, 11570–11578.

[16] G. R. Fulmer, A. J. M. Miller, N. H. Sherden, H. E. Gottlieb, A. Nudelman, B. M. Stoltz, J. E. Bercaw, K. I. Goldberg, *Organometallics* **2010**, *29*, 2176–2179.

[17] A. J. Arduengo, H. V. R. Dias, R. L. Harlow, M. Kline, *J. Am. Chem. Soc.* **1992**, *114*, 5530–5534.

[18] V. M. Marx, M. B. Herbert, B. K. Keitz, R. H. Grubbs, *J. Am. Chem. Soc.* **2013**, *135*, 94–97.

[19] J.-E. Jee, J. L. Cheong, J. Lim, C. Chen, S. H. Hong, S. S. Lee, *J. Org. Chem.* **2013**, *78*, 3048–3056.

[20] J. R. Bruckner, J. Bauhof, J. Gebhardt, A.-K. Beurer, Y. Traa, F. Giesselmann, *J. Phys. Chem. B* **2021**, *125*, 3197–3207.

[21] E. Welter, R. Chernikov, M. Herrmann, R. Nemausat, *AIP Conf. Proc.* **2019**, *2054*, 040002.

[22] B. Ravel, M. Newville, *J. Synchrotron Radiat.* **2005**, *12*, 537–541.

[23] M. Thommes, K. Kaneko, A. V. Neimark, J. P. Olivier, F. Rodriguez-Reinoso, J. Rouquerol, K. S. W. Sing, *Pure Appl. Chem.* **2015**, *87*, 1051–1069.

Manuscript received: July 12, 2023
Revised manuscript received: September 6, 2023
Accepted manuscript online: September 7, 2023
Version of record online: September 27, 2023